LETTER

Stressing Halide Perovskites with Light and Electric Fields

Sarah Wieghold,* Emily M. Cope, Gregory Moller, Nozomi Shirato, Burak Guzelturk, Volker Rose, and Lea Nienhaus*

Read Online

ACCESS | Metrics & More | Article Recommendations | SI Supporting Information

ABSTRACT: Understanding the light and electric field-induced effects underlying the local changes in optoelectronic properties in lead halide perovskites is crucial to establish a detailed structure−function relationship. Here, we use single-molecule absorption scanning tunneling microscopy (SMA-STM) to probe the local surface inhomogeneity of a mixed A-site cation/mixed halide perovskite under pulsed 532 nm photoexcitation to gain insight into the varying grain-to-grain absorption behavior at the nanoscale and reduction in the electronic bandgap under illumination. To correlate the observed changes in the absorption signal to structural ones, we utilize synchrotron X-ray STM (SX-STM) where we find that photoexcitation induces changes in the X-ray absorption spectral signatures. Lastly, using pump−probe time-resolved wide-angle X-ray scattering, we show the presence of nonthermal lattice deformations upon photoexcitation which indicate that the excited photocarriers distort the perovskite lattice, corroborating the local electronic changes observed by our STM measurements.
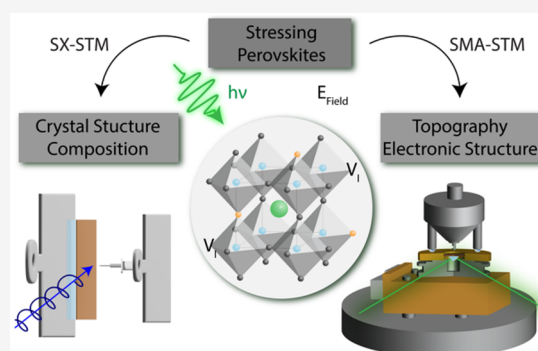
Organic−inorganic perovskite solar cells have emerged over the last couple of years because of their unprecedented optoelectronic properties.[1−3] However, several questions regarding the impact of optical illumination and an electric voltage on the underlying structural change of the perovskite absorber layer remain unanswered.[4−9] Ensemble studies have shown that the voltage sweep direction severely affects the transient hysteretic behavior caused by ionic movement.[6,9−12] Further, low voltages can have a positive impact on the film stability, while applied voltages larger than the built-in potential (or open-circuit voltage, V_{OC}) induce reversible and/or irreversible degradation of the perovskite material.[6,7,13,14] On the other hand, illumination can induce phase segregation in mixed halide systems which in term affects the optical properties, resulting in, for example, a redshift of the emission wavelength.[15−19] However, to fully identify the root cause of changes of the optoelectronic properties due to structural changes of the perovskite absorber layer under electric fields and illumination, a combined approach is necessary.

To unravel the underlying mechanisms associated with material stability under external stimuli, scanning probe microscopy (SPM) techniques offer a unique opportunity to image material systems down to the nanoscale and to visualize dynamics locally at the material interface.[20,21] For example, conductive atomic force microscopy (cAFM) and Kelvin probe

force microscopy (KPFM) have indicated that the perovskite photoconductivity is influenced by film thickness and grain alignment,[22−24] or grain boundary type,[25] affecting the overall performance output. By performing illuminated heterodyne KPFM experiments, quasi-Fermi level splitting and local variations in the V_{OC} across a MAPbI$_3$ (MA = methylammonium) film were spatially and temporally resolved giving insight into real-time voltage dynamics.[26] For a mixed A-site, mixed halide perovskite [(FAPbI$_3$)$_{0.85}$(MAPbBr$_3$)$_{0.15}$, FA = formamidinium], strain disorder was generated under light and an applied bias.[16]

Scanning tunneling microscopy (STM) in combination with scanning tunneling spectroscopy (STS) extends the SPM capabilities and allows for atomic resolution imaging of, for example, MAPbBr$_3$ single crystals, MAPbI$_3$ on Au(111), and mixed halide perovskites MAPb(Br$_{3−x}$I$_x$)$_3$.[27−29] It was further shown that the intensity of the local density of states (LDOS) increases under optical illumination and a shift in the conduction band (CB) onset occurred because of additional

free carriers and new tunneling pathways.[27] The influence of different surface passivation of a MAPbI$_3$ thin film by STS revealed differences in the amount of surface states due to changes in the Fermi-level pinning likely affecting the optoelectronic properties in thin films.[30]

To investigate the nanoscale properties of a lead halide perovskite thin film, Cs$_{0.05}$(FA$_{0.83}$MA$_{0.17}$)$_{0.95}$Pb(I$_{0.83}$Br$_{0.17}$)$_3$ (termed CsFAMA in the following), under optical excitation, we use a modified approach based on single-molecule absorption STM (SMA-STM).[31] CsFAMA was chosen because of its higher stability under stressors, such as temperature and illumination, compared to bare organic halide perovskites which readily degrade and decompose.[4] SMA-STM is based on electronic detection of optical absorption processes using the STM tip as a local probe. It takes advantage of a change in the LDOS population based on the excitation of an electron upon photon absorption. By dithering the excitation laser faster than the tip feedback loop, an additional "photocurrent" modulation is obtained and can be detected by lock-in amplifier.[32−34] Local heating is avoided because of a back-illumination geometry, thus allowing for STM measurements under stable tip conditions.[33−36] In this unique light coupling geometry, photoexcitation occurs via the evanescent field resulting from total internal reflection (Kretschmann configuration).[37] Strong field enhancement in the presence of the sharp STM metal tip aids in achieving a sufficient optical absorption signal for detection.[33,38] Using this approach, carbon nanotubes,[32,33] PbS quantum dots,[34,39] organic molecules,[40] and plasmonic excitations[41,42] have been successfully investigated.

Here, we take advantage of the SMA-STM technique and add a 532 nm picosecond pulsed diode laser as the excitation source (Figure 1a). With this approach, STS can be performed in the dark and under illumination (Figure 1b). A topography of the CsFAMA film under 532 nm photoexcitation is shown in Figure 1c, highlighting that illumination does not influence the scanning quality and confirming that sample heating is not a major issue in this back-illumination geometry of the STM tip−sample junction.

To demonstrate the fundamental principle of room-temperature SMA-STM, Figure 1d shows the different tunneling pathways in the dark and under illumination (532 nm illumination is highlighted in green) when tunneling from the sample to the tip. In the dark, electrons in filled states of the sample can tunnel into empty states in the tip, as determined by the tip and sample Fermi levels ($E_{F,S}$; $E_{F,T}$) shifted by the applied bias (eV). Because of expected plasmonic excitation of the PtIr tip by scattered light under illumination, the population of the DOS of the tip will be slightly modified, leading to a "higher electron temperature", and thus a change in the electron distribution around E_F. In the perovskite on the other hand, optical excitation results in the promotion of electrons from the valence band (VB) to the CB, thus resulting in a wider range of energies populated by electrons, enabling new tunneling pathways.

To gain insight into the current−voltage characteristics, we perform STS measurements. We start the STS measurements without illumination to distinguish between changes induced by the applied electric field and illumination. Figure S1 shows the spectra without illumination for several set point voltages and a tunneling current of 100 pA. An electric field (E_{field}) effect is observed with the following dependence: $E_{field} = V/d$, where V is the applied bias and d is the distance between the
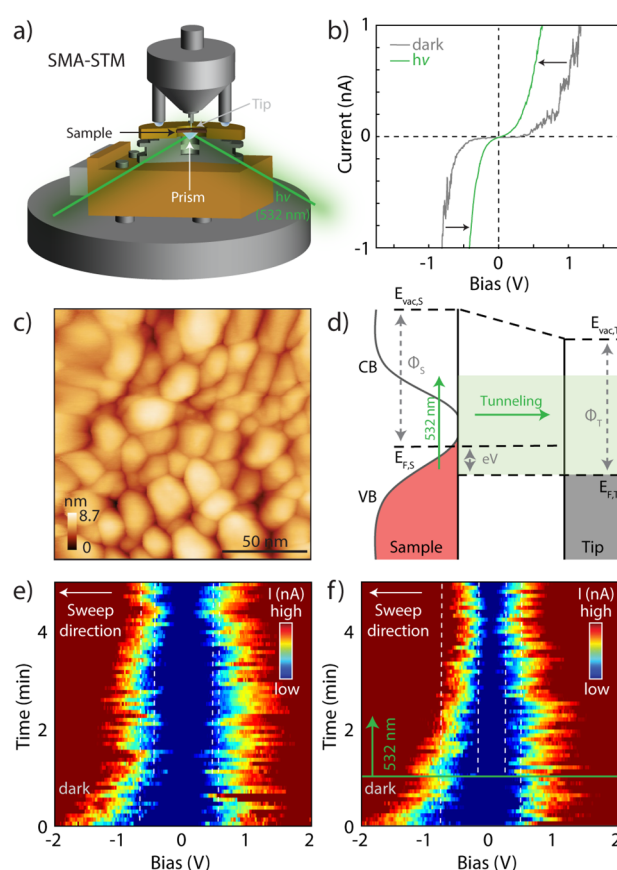

Figure 1. (a) Schematic of the SMA-STM setup using the back illumination geometry. (b) I−V curves acquired without (gray) and under 532 nm illumination (green). The black arrows highlight the narrowing of the bandgap under illumination. (c) STM topography of CsFAMA under 532 nm illumination. Scanning conditions: −0.8 V, 100 pA. (d) Tunneling pathways under illumination from the sample to the tip. (e) Time evolution of the bandgap without illumination. (f) Time evolution of the bandgap under 532 nm excitation. The green line indicates when the laser was switched on, and the white dashed lines are a guide to the eye to highlight the narrowing of the bandgap.

tip and the sample. At higher tunneling currents, the tip is closer to the surface (smaller d), thus increasing the electric field at each point during the voltage sweep which manifests as an overall smaller apparent electronic bandgap. These results also highlight that the observed effect is not due to tip-induced band bending, where an opposite trend would be expected (Figure S2).

When we compare the STS acquired in the dark and under 532 nm excitation (Figure 1b), we observe a reduction in the apparent electronic bandgap under illumination. This expected effect can be attributed to new tunneling pathways as well as to additional free carriers generated under illumination contributing to the tunneling process.[27,33] To further highlight this effect, we investigate the time evolution of the electronic bandgap by STS without illumination (Figure 1e) and under 532 nm illumination (Figure 1f) by repeated sampling (see Figures S3 and S4 for additional I−V curves with varying sweep directions). Over a time interval of 5 min the apparent electronic bandgap of CsFAMA slightly reduces without illumination. Upon continuous illumination (indicated by the green line in Figure 1f), the reduction is much more pronounced.

In general, there are several plausible explanations for the underlying root cause of an electronic bandgap reduction: (i) a simple quadratic Stark shift[43] which also has been shown to be able to close the apparent bandgap in semiconducting CNTs;[33] (ii) a change in the underlying perovskite composition due to ion migration and possible phase segregation; and (iii) structural changes in the perovskite lattice due to rotation or tilting of the PbI_6^{4-} octahedron and/or changes in the bond lengths and nearest-neighbor distance.

However, we can rule out a simple Stark shift due to a gradually decreasing bandgap over time (*e.g.*, minutes) under an applied electric field (see Figure 1e) rather than an instantenous continuous effect. We formulate the following hypothesis by converging on the other two listed possibilities for the observed electronic bandgap reduction. Under an electric field, it has been shown that positively or negatively charged ions or vacancies can migrate because of the ionic nature of the octahedral sublattice.[44] Particularly, shallow and deep trap states can be created under applied electric fields, effectively shifting the VB and CB onsets. This shift results in a modification of the LDOS available for tunneling. This process can be further enhanced under illumination where the additional photogenerated free charge carriers contribute to the tunneling process, open up new tunneling pathways, as well as increase ion mobility through photoinduced lattice deformations.[27,45,46] Thus, we hypothesize that electric fields and optical illumination change the amount and overall defect polarity at the interface. Taking this assumption one step further, these changes imply that the perovskite lattice becomes distorted under the added external stimuli, which would result in octhedral elongation or compression.

Thus far, we have investigated the response of the perovskite to different stimuli. However, one remaining question is how the local CsFAMA behavior changes from grain to grain across the surface. Figure 2a shows the STM topography where several large grains ∼200−250 nm in diameter are seen which are composed of smaller grain structures (see Figure S5 for a comparative scanning electron micrograph and AFM topography of the same CsFAMA thin film). We extract a root-mean-square value of ∼2 nm indicating a smooth surface. We further performed differential tunneling conductance (dI/dV) mapping to investigate the homogeneity of the conductance of our perovskite surface (Figure S6).

To demonstrate the strength of SMA-STM, we begin the measurement in the dark and then switch the laser on to extract the photomodulated tunneling component which corresponds to the optical absorption signal via lock-in amplifier (Figure 2b; the green line pointing downward indicates laser is on). We find a strong response of the modulated tunneling current signal (SMA-STM color scale; black, current < 1 pA; white, current > 10 pA); compare also Figure 2c for the extracted photomodulated component when the tip is held in tunneling range at a random location. Figure 2d shows a map of the optical absorption signal under pulsed 532 nm excitation which can be obtained simultaneously with the topography image shown in Figure 2a. Upon illumination, we find regions that show a strong signal (white) and nanoscale grains which show a weaker signal (gray/black). Figure 2e shows the current distribution extracted from the lock-in image of the optical absorption in Figure 2d. Interestingly, we find a broad distribution of optical absorption signals with two local maxima at 5 and 16 pA, indicating regions of stronger and weaker interaction with the laser.
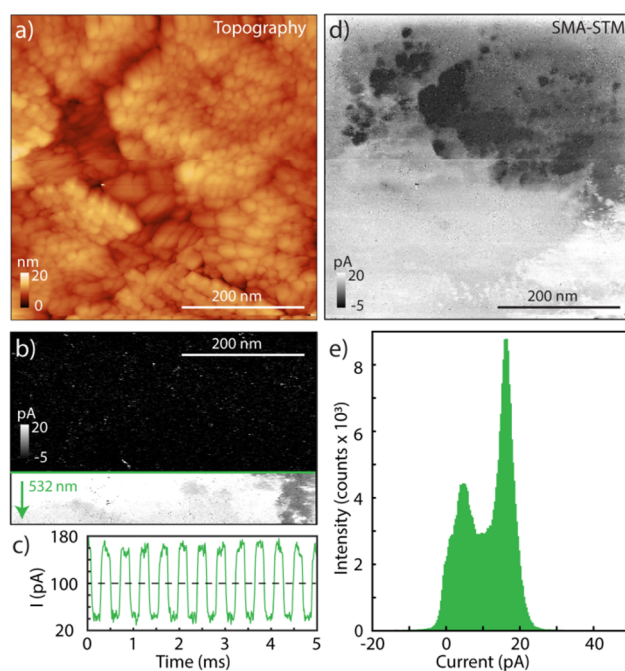

Figure 2. (a) STM topography image of CsFAMA. (b) SMA-STM image collected in the dark (upper half). The green line indicates when the 532 nm laser is switched on (bottom half). Dark signal, <1 pA; white signal, >10 pA. (c) Photomodulated tunneling component. (d) SMA-STM image under 532 nm illumination showing areas with high (white, >10 pA) and lower (gray, <1 pA) signal. (e) Histogram of lock-in pixel intensities from panel d. STM scanning conditions: −0.8 V, 100 pA.

One condition of achieving a strong SMA-STM signal is that the incident optical excitation power must saturate the optical transition and shift the equilibrium to the excited state.[47] The saturation intensity, I_s, under tip-field enhancement, f, for an optical transition with lifetime, τ_r, excited at a wavelength, λ, is[38]

$$I_s = \frac{2\sqrt{2}\,hc}{f^2\,\pi\tau_r\lambda^3} \tag{1}$$

Based on this relationship, regions with a shorter photoluminescence lifetime (due to rapid, trap-assisted nonradiative recombination) would require a higher incident excitation power to fully saturate the transition and, therefore, show a weaker SMA-STM signal, as an average between the excited state and ground state will be observed.

To align these results with our previous hypothesis, lattice distortions induced by electric fields or optical illumination might change the overlap integral between energy eigenstates; hence, a reduced SMA-STM signal can also be expected because of structural changes in addition to changes due to a purely optical excitation. An alteration of the overlap integral can also change the tunneling probability. Additionally, if the local composition changes slightly because of, for example, halide migration resulting in locally different I/Br ratios or the presence of ionic interstitials or vacancies, the overlap between the utilized excitation and an optically allowed transition may differ. Such defect states might be also the reason for rapid excited-state recombination, which is known to reduce the extracted SMA-STM signal intensity.

Thus, to understand and clarify if and how the structure of CsFAMA changes under the additional stimuli of electric fields
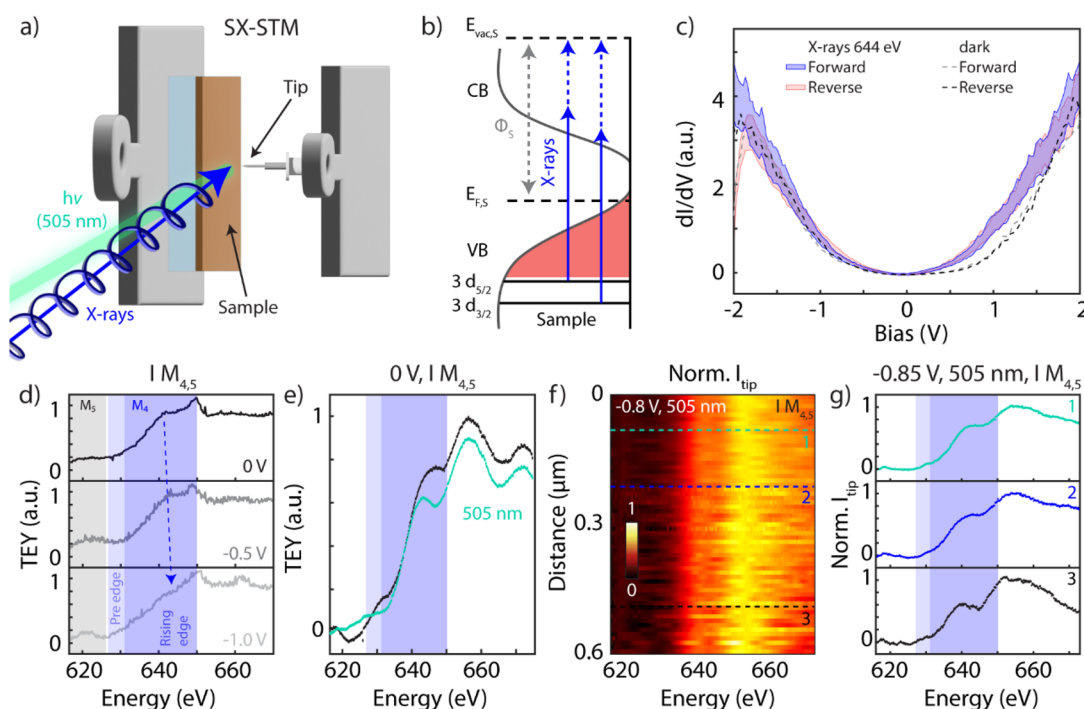
Figure 3. (a) Schematic of the SX-STM setup. (b) Schematic of the tunneling pathways under X-ray illumination. (c) dI/dV spectra without and under 644 eV X-ray excitation. The average is shown without X-ray illumination (dashed lines), while the shaded region highlights the upper and lower bound of the confidence interval under 644 eV X-rays. (d) TEY XAS at the I $M_{4,5}$ edge for varying applied voltages (0 V, black; −0.5 V, gray; −1.0 V, light gray). The shaded regions highlight the M_5 edge (gray) and M_4 pre-edge and edge (blue), respectively. (e) TEY XAS at the I $M_{4,5}$ edge without (black) and under 505 nm (cyan) optical excitation at 0 V. (f) 2D plot of the XAS measured at the STM tip under 505 nm optical excitation as a function of location. The intensity of the XAS is plotted as the Z axis from low (red) to high (yellow). The spectra were recorded in tunneling range at −0.8 V and 100 pA. (g) Extracted absorption spectra at the location marked by the cyan, blue, and black dashed lines in panel e.

and laser excitation, we use SX-STM at the beamline 4-ID-E of the Advanced Photon Source (APS) and the Center for Nanoscale Materials (CNM) at Argonne National Laboratory with and without illumination (see schematic in Figure 3a,b).[48] In SX-STM, a coaxial coated STM smart tip is held in tunneling range (near-field mode) or approximately 1 μm above the sample surface (far-field mode) and a monochromatic synchrotron X-ray beam with a size of ∼10 μm × 10 μm illuminates the tip/sample junction in ultrahigh vacuum. Operated in the soft X-ray regime, we probe the iodine $3d_{3/2}$ and $3d_{5/2}$ transitions at the M_4 and M_5 edge, respectively. Here, the final states that are probed by the $M_{4,5}$ absorption edges are of p and f character while the initial states are split because of the spin−orbit coupling into $3d_{3/2}$ and $3d_{5/2}$. We focus on the change in the iodine edge in our SX-STM measurements because it has been shown that iodine has the lowest activation energy and hopping barrier among intrinsic defects within a mixed halide perovskite lattice.[49]

We begin by measuring the change in the differential tunneling conductance, dI/dV, across the CsFAMA interface under 644 eV (M_4) resonant X-ray excitation. To obtain results comparable to those of the SMA-STM, we set the same initial tunneling conditions of −0.8 V and 100 pA. Figure 3c shows the averaged dI/dV without (dashed line) and under 644 eV X-ray excitation (solid line) for the forward and reverse sweep directions. For statistics, we averaged 100 spectra without illumination and approximately 350 spectra under 644 eV excitation across a 300 × 300 nm^2 grid. The high and low bounds of the confidence interval under X-ray excitation are shown as shaded areas. We find a major change in the CB

onset while the VB onset is only slightly shifted compared to the dI/dV without illumination. These results can be explained in light of the schematic shown in Figure 3b: under X-ray excitation, additional tunneling pathways open up at a positive voltage because of the change in the LDOS occupation probability.

To probe the change in the local geometric and electronic structure under illumination and applied electric fields, X-ray absorption spectroscopy (XAS) via SX-STM is used in the following to investigate the change in the pre-edge, rising, and main edge absorption features at the I $M_{4,5}$ edge. First, we measure the total electron yield (TEY) which is caused by the X-ray beam illuminating the sample. In this mode, a sample current is generated by excitation of primary and secondary electrons to empty states above the Fermi or vacuum level ($I_{Sample} \propto TEY_{average}$). Figure 3d shows the TEY spectra measured under negative voltages ranging from 0 V to −1 V without optical excitation. We find that the structure and position of the $M_{4,5}$ absorption onset remains the same when operated under these low-voltage conditions. However, we find that the rising edge feature shifts to higher energies under higher negative voltages.

To uncover the influence of optical excitation on the structural change, Figure 3e depicts the TEY spectra without (black) and under continuous 505 nm excitation using a 170 mW light-emitting diode at 0 V applied bias. The overall absorption edge is similar in both cases; however, stark variations are observed for the pre-edge and location of the rising edge feature (M_4). It has been previously shown that tilted octahedra in the perovskite structure can redshift and

broaden the rising edge feature by probing the Pb $L_{2,3}$ edge.[50] Illumination can generate an additional transition in the excited-state XAS which can blueshift the absorption onset because of localized photogenerated holes in a Br-based perovskite.[51] A change in the nearest-neighbor distance for the I—I bond has also been reported, attributed to octahedral rotation under illumination.[52]

According to the TEY data, the small shift in the absorption onset is based on competing processes consisting of a tilted PbX_6^{4-} octahedra (redshift) and localized hole generation (blueshift). Additionally, we attribute the changes and broadening seen in the rising and main edge to distorted octahedral changes (elongation) impacting the overall iodine—iodine bond length.

The question now arises: how does the electronic structure change at the nanometer scale across the CsFAMA surface? Thus, in a second experiment, we take advantage of the SX-STM method and bring the STM smart tip in tunneling range at a voltage of −0.8 V and 100 pA. In this configuration, an X-ray excited tunneling portion (I_{tip}) can be extracted using a lock-in amplifier.[53] To obtain the local structural change, we measure XAS every 10 nm in tunneling range for a total distance of 0.6 μm under 505 nm illumination. Figure 3f shows a two-dimensional plot of the XAS (intensity in Z direction) where the photon energy is plotted as a function of location. We find that across the measured distance, the M_4 absorption onset does not shift as seen by three representative spectra (Figure 3g; location of the XAS is marked by the dotted lines in Figure 3f). However, we observe slight changes in the rising edge depending on the location at the surface, indicating local inhomogeneities across the film.

To correlate possible structural responses with photoexcitation, we also perform time-resolved wide-angle X-ray scattering (TR-WAXS) measurements in a pump—probe configuration at beamline 11-ID-D at APS. Because of experimental constraints, we had to use a different excitation wavelength, i.e., 400 nm, replacing the 532 and 505 nm used in the earlier parts. Although this may induce small subtleties due to differences in hot carrier generation, we expect that the main structural responses to an above-bandgap photoexcitation would be comparable. Figure 4a shows the static diffraction intensity ($I(Q)$) up to a momentum transfer range of Q = 3.3 Å^{-1} (experimental Q_{max} here is 5.3 Å^{-1}). We identify the Bragg reflection associated with the cubic structure of CsFAMA without any additional impurity compositions present (e.g., PbI_2 or CsI); hence, the sample is phase pure. The blue and black curves in Figure 4a show the differential changes in the scattering intensity when excited with the laser for a pump—probe delay of −60 and 100 ns. There is no change in the scattering intensity in the case of t = −60 ns because the X-ray probe arrives earlier than the optical pump. Hence, the sample is already in its ground state, indicating no lattice distortions. However, there is a clear differential signal at a delay time of t = 100 ns. The transient differential response is derivative in shape with a peak on the low Q side and dip on the high Q side, indicating that the Bragg peaks transiently shift to lower Q; hence, the lattice expands under illumination.

The underlying mechanism of the transient response needs further elaboration, which could arise from thermal energy deposited by the relaxation of hot carriers and/or carrier-induced local lattice deformations.[52,54] A closer look into the transient diffraction intensity (blue curve in Figure 4a) indicates that the dip features are commonly stronger than
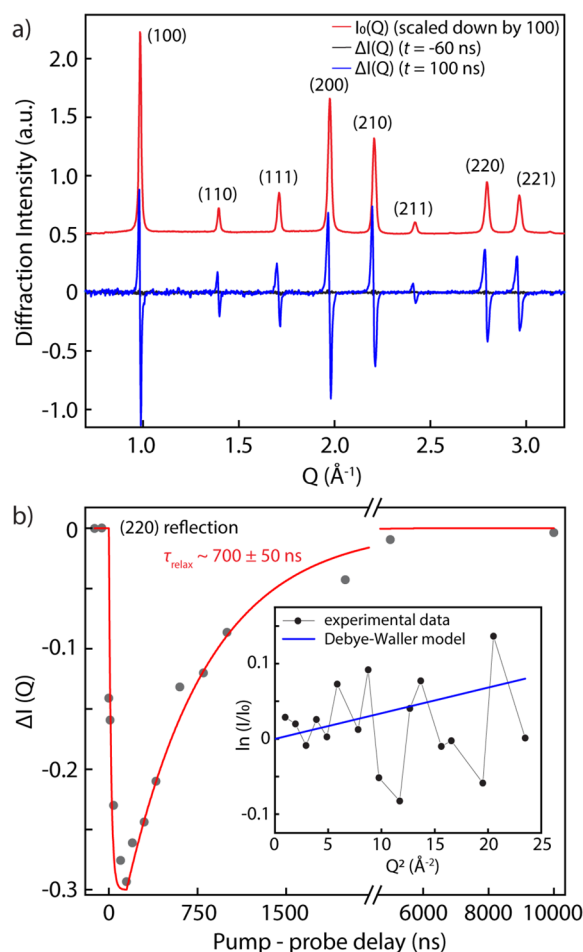

Figure 4. (a) Static diffraction intensity ($I(Q)$) (red) and differential change in the scattering intensity for a laser pump—probe delay of −60 ns (black) and 100 ns (blue). (b) Temporal dynamics of the transient lattice response for the (220) reflection. Inset: comparison of the transient response of the experimental data and the Debye—Waller model.

the peak features. This observation mainly arises from the fact that the sample transiently heats up because of hot-carrier relaxation; hence, the sample becomes slightly more disordered as the mean squared displacement of the atoms increase. The Debye—Waller model, or temperature model, accounts for the changes in the mean squared displacements versus the diffraction intensity. In this model, $-\ln\left(\frac{I(Q,t)}{I_0(Q)}\right) = \frac{1}{3}Q^2\langle\Delta u(t)^2\rangle$ where Q is the scattering vector, $I(Q,t)$ the diffraction intensity at a pump—probe delay t, $I_0(Q)$ the diffraction intensity in the absence of laser excitation, and $\langle\Delta u(t)^2\rangle$ the induced atomic mean squared displacements. In the Debye-Waller model, there is a Q^2 dependence indicating that Bragg peaks at higher Q (or 2θ) experience a larger intensity loss due to a temperature increase.[55] To investigate the temperature increase-induced disordering, the experimental data is plotted as $-\ln\left(\frac{I}{I_0}\right)$ over Q^2 in the inset of Figure 4b. Although the general trend suggests a Debye-Waller-like response (solid line), particular Bragg peaks strongly deviate. For example, Bragg peaks at Q = 1.71 Å^{-1}, (111) reflection, and Q = 3.42 Å^{-1}, (222)

reflection, show overall an increase of the Bragg peak intensity transiently. This points out the role of nonthermal lattice deformations induced by the presence of charge carriers either changing the octahedral tilt or local bonding at the unit cell level. Therefore, the experimental data strongly deviates from a simple thermal response indicating that the transient structural response is strongly affected by the local deformations of the perovskite lattice due to the presence of photogenerated charge carriers.

Furthermore, we resolve the temporal dynamics of the transient lattice response. Figure 4b shows the dynamics measured for the (220) reflection. The relaxation of the photoinduced structural expansion exhibits a characteristic relaxation time $\tau_{\text{relax}} = 700 \pm 50$ ns at an excitation fluence of 150 μJ cm^{-2}, which is comparable to the charge carrier lifetime of this material (Figure S7). The other probed Bragg peaks also exhibit similar temporal dynamics (Figure S8).

Previously, we hypothesized that the obtained SMA-STM signal can be in part related to structural changes under optical illumination, which in turn influence the tunneling probability. By measuring XAS at the I M$_{4,5}$ edge coupled with TR-WAXS, we conclude that carrier-induced lattice deformations are present, which dynamically modify the electronic properties in halide perovskites. One possible explanation which we already mentioned earlier in the text is related to defects which can be manipulated because of the intrinsic built-in potential of perovskites as well as by externally applied electric fields. Specifically, charged defects exhibit a preferential migration direction under such fields where the interfacial properties are influenced because of accumulation of defects with a certain polarity. Here, cross-sectional STM has shown previously that the potential energy landscape is modified under illumination for MAPbBr$_3$.[46] Particularly, under illumination a reordering of the organic cation dipoles occurs creating one-dimensional potential energy wells for electrons and holes. These pathways are aligned, for example, along the [110] direction and influence carrier transport. Specifically, because of the reordering and creation of pathways, the probability that electrons and holes recombine is reduced, thus leading to an increase in carrier lifetime. Our study indicates that such charge defects, in addition to the generated charge carriers under illumination, are responsible for a change in the perovskite structure as shown by our XAS measurements. Changes in the rising and main edge features further give rise to speculations that the perovskite structure becomes distorted in addition to changes in the I−I bond length possibly due to vacancies.

We also show that the underlying iodine environment of the perovskite changes locally across the CsFAMA surface. One possible scenario might be related to slight changes in the chemical composition which in turn influence the XAS behavior under illumination for the single grains. This hypothesis is further underpinned by the results of our SMA-STM measurements. Particularly, we see changes in the optical absorption signal which hint that the overlap between the utilized excitation and an optically allowed transition may differ. In addition, structural changes upon optical illumination or application of an electric field are expected to change the electron−phonon coupling, which in turn will influence the carrier recombination dynamics, which are a key part of the observed SMA-STM signal according to eq 1. However, we note that first-principles density functional theory calculations are necessary to unambiguously determine the exact under-

lying structural and compositional change and also determine the nature and influence of defects which will be of interest in future studies.

In conclusion, the combination of STM-based techniques with electromagnetic radiation shows great potential in unraveling the underlying optoelectronic changes in perovskite materials under various stimuli, e.g., illumination, electric fields, temperature, or a combination thereof. Compared to other techniques which are diffraction-limited, the presented approach uses the STM tip as a "detector" for the absorption signal in SMA-STM and SX-STM experiments; hence, the absorption signature can be detected down to the single-atom level. This might be also of interest for future emerging material systems, such as two-dimensional Ruddlesden−Popper hybrid perovskites which show great promise as quantum well structures.[56,57]

In summary, we have investigated the influence of an applied electric field and light illumination on the underlying changes in the optoelectronic properties of a CsFAMA perovskite film. We find that the bare impact of the electric field on the current−voltage behavior already changes its response in addition to a slight reduction in the bandgap over time. This effect becomes strongly enhanced when photoexcitation is added. By using SMA-STM, we show that there are significant local variations in the absorption behavior of the CsFAMA perovskite film across the interface. Using a combined SX-STM and TR-WAXS approach, we could further pinpoint the root cause to structural changes within the perovskite layer. Photogenerated charge carriers distort the perovskite lattice, corroborating the local electronic changes observed by our STM measurements. This study shows the importance of performing nanoscale characterization experiments coupled to time-resolved spectroscopy techniques to fully unravel the mechanisms underlying the changes in the optoelectronic properties in halide perovskites under external stimuli.

■ ASSOCIATED CONTENT

ⓢ Supporting Information

The Supporting Information is available free of charge at https://pubs.acs.org/doi/10.1021/acsenergylett.2c00866.

> Experimental section, current−voltage spectra of varying set point currents and voltages, time evolution of the bandgap with and without illumination, dI/dV map, lifetime of CsFAMA, and additional temporal dynamics of the transient lattice response (PDF)

■ AUTHOR INFORMATION

Corresponding Authors

Sarah Wieghold − *Department of Chemistry and Biochemistry, Florida State University, Tallahassee, Florida 32306, United States; X-ray Science Division, Advanced Photon Source and Center for Nanoscale Materials, Argonne National Laboratory, Lemont, Illinois 60439, United States*; Email: swieghold@anl.gov

Lea Nienhaus − *Department of Chemistry and Biochemistry, Florida State University, Tallahassee, Florida 32306, United States;* ⓞ orcid.org/0000-0003-1412-412X; Email: lnienhaus@fsu.edu

Authors

Emily M. Cope − *Department of Chemistry and Biochemistry, Florida State University, Tallahassee, Florida 32306, United States;* ⓘ orcid.org/0000-0002-1539-6656

Gregory Moller − *Department of Chemistry and Biochemistry, Florida State University, Tallahassee, Florida 32306, United States;* ⓘ orcid.org/0000-0002-9577-4767

Nozomi Shirato − *Center for Nanoscale Materials, Argonne National Laboratory, Lemont, Illinois 60439, United States*

Burak Guzelturk − *X-ray Science Division, Advanced Photon Source, Argonne National Laboratory, Lemont, Illinois 60439, United States;* ⓘ orcid.org/0000-0003-1977-6485

Volker Rose − *X-ray Science Division, Advanced Photon Source and Center for Nanoscale Materials, Argonne National Laboratory, Lemont, Illinois 60439, United States*

Complete contact information is available at:
https://pubs.acs.org/10.1021/acsenergylett.2c00866

Notes

The authors declare no competing financial interest.

■ REFERENCES

(1) Saliba, M.; Matsui, T.; Seo, J.-Y.; Domanski, K.; Correa-Baena, J.-P.; Nazeeruddin, M. K.; Zakeeruddin, S. M.; Tress, W.; Abate, A.; Hagfeldt, A.; Grätzel, M. Cesium-Containing Triple Cation Perovskite Solar Cells: Improved Stability, Reproducibility and High Efficiency. *Energy Environ. Sci.* **2016**, *9* (6), 1989−1997.

(2) Yoo, J. J.; Wieghold, S.; Sponseller, M. C.; Chua, M. R.; Bertram, S. N.; Hartono, N. T. P.; Tresback, J. S.; Hansen, E. C.; Correa-Baena, J.-P.; Bulović, V.; Buonassisi, T.; Shin, S. S.; Bawendi, M. G. An Interface Stabilized Perovskite Solar Cell with High Stabilized Efficiency and Low Voltage Loss. *Energy Environ. Sci.* **2019**, *12* (7), 2192−2199.

(3) Stranks, S. D.; Eperon, G. E.; Grancini, G.; Menelaou, C.; Alcocer, M. J. P.; Leijtens, T.; Herz, L. M.; Petrozza, A.; Snaith, H. J. Electron-Hole Diffusion Lengths Exceeding 1 Micrometer in an Organometal Trihalide Perovskite Absorber. *Science* **2013**, *342* (6156), 341−344.

(4) Wieghold, S.; Bieber, A. S.; Mardani, M.; Siegrist, T.; Nienhaus, L. Understanding the Effect of Light and Temperature on the Optical Properties and Stability of Mixed-Ion Halide Perovskites. *J. Mater. Chem. C* **2020**, *8* (28), 9714−9723.

(5) Wieghold, S.; Shirato, N.; Rose, V.; Nienhaus, L. Investigating the Effect of Electric Fields on Lead Halide Perovskites by Scanning Tunneling Microscopy. *J. Appl. Phys. Phys.* **2020**, *128*, 125303.

(6) Bae, S.; Kim, S.; Lee, S.-W.; Cho, K. J.; Park, S.; Lee, S.; Kang, Y.; Lee, H.-S.; Kim, D. Electric-Field-Induced Degradation of Methyl-ammonium Lead Iodide Perovskite Solar Cells. *J. Phys. Chem. Lett.* **2016**, *7* (16), 3091−3096.

(7) Leijtens, T.; Hoke, E. T.; Grancini, G.; Slotcavage, D. J.; Eperon, G. E.; Ball, J. M.; De Bastiani, M.; Bowring, A. R.; Martino, N.; Wojciechowski, K.; McGehee, M. D.; Snaith, H. J.; Petrozza, A. Mapping Electric Field-Induced Switchable Poling and Structural Degradation in Hybrid Lead Halide Perovskite Thin Films. *Adv. Energy Mater.* **2015**, *5* (20), 1500962.

(8) Ji, D.; Na, M.; Wang, S.; Zhang, H.; Zhu, K.; Zhang, C.; Li, X. Role of an External Electric Field on Hybrid Halide Perovskite CH3NH3PbI3 Band Gaps. *Sci. Rep.* **2018**, *8* (1), 12492.

(9) Tress, W.; Marinova, N.; Moehl, T.; Zakeeruddin, S. M.; Nazeeruddin, M. K.; Grätzel, M. Understanding the Rate-Dependent J−V Hysteresis, Slow Time Component, and Aging in CH3NH3PbI3 Perovskite Solar Cells: The Role of a Compensated Electric Field. *Energy Environ. Sci.* **2015**, *8* (3), 995−1004.

(10) Snaith, H. J.; Abate, A.; Ball, J. M.; Eperon, G. E.; Leijtens, T.; Noel, N. K.; Stranks, S. D.; Wang, J. T.-W.; Wojciechowski, K.; Zhang, W. Anomalous Hysteresis in Perovskite Solar Cells. *J. Phys. Chem. Lett.* **2014**, *5* (9), 1511−1515.

(11) Xiao, Z.; Yuan, Y.; Shao, Y.; Wang, Q.; Dong, Q.; Bi, C.; Sharma, P.; Gruverman, A.; Huang, J. Giant Switchable Photovoltaic Effect in Organometal Trihalide Perovskite Devices. *Nat. Mater.* **2015**, *14* (2), 193−198.

(12) Li, C.; Tscheuschner, S.; Paulus, F.; Hopkinson, P. E.; Kießling, J.; Köhler, A.; Vaynzof, Y.; Huettner, S. Iodine Migration and Its Effect on Hysteresis in Perovskite Solar Cells. *Adv. Mater.* **2016**, *28* (12), 2446−2454.

(13) Wu, J.; Li, Y.; Tan, S.; Yu, B.; Li, H.; Li, Y.; Shi, J.; Wu, H.; Luo, Y.; Li, D.; Meng, Q. Enhanced Perovskite Solar Cell Efficiency Via the Electric-Field-Induced Approach. *ACS Appl. Mater. Interfaces* **2020**, *12* (24), 27258−27267.

(14) Li, X.; Wang, X.; Zhang, W.; Wu, Y.; Gao, F.; Fang, J. The Effect of External Electric Field on the Performance of Perovskite Solar Cells. *Org. Electron.* **2015**, *18*, 107−112.

(15) Brennan, M. C.; Draguta, S.; Kamat, P. V.; Kuno, M. Light-Induced Anion Phase Segregation in Mixed Halide Perovskites. *ACS Energy Lett.* **2018**, *3* (1), 204−213.

(16) Kim, D.; Yun, J. S.; Sharma, P.; Lee, D. S.; Kim, J.; Soufiani, A. M.; Huang, S.; Green, M. A.; Ho-Baillie, A. W. Y.; Seidel, J. Light- and Bias-Induced Structural Variations in Metal Halide Perovskites. *Nat. Commun.* **2019**, *10* (1), 444.

(17) Hoke, E. T.; Slotcavage, D. J.; Dohner, E. R.; Bowring, A. R.; Karunadasa, H. I.; McGehee, M. D. Reversible Photo-Induced Trap Formation in Mixed-Halide Hybrid Perovskites for Photovoltaics. *Chem. Sci.* **2015**, *6* (1), 613−617.

(18) Slotcavage, D. J.; Karunadasa, H. I.; McGehee, M. D. Light-Induced Phase Segregation in Halide-Perovskite Absorbers. *ACS Energy Lett.* **2016**, *1* (6), 1199−1205.

(19) Yoon, S. J.; Draguta, S.; Manser, J. S.; Sharia, O.; Schneider, W. F.; Kuno, M.; Kamat, P. V. Tracking Iodide and Bromide Ion Segregation in Mixed Halide Lead Perovskites during Photo-irradiation. *ACS Energy Lett.* **2016**, *1* (1), 290−296.

(20) Wieghold, S.; Nienhaus, L. Probing Semiconductor Properties with Optical Scanning Tunneling Microscopy. *Joule* **2020**, *4* (3), 524−538.

(21) Wieghold, S.; Nienhaus, L. Nanoscale Properties of Lead Halide Perovskites by Scanning Tunneling Microscopy. *EcoMat* **2021**, *3* (2), No. e12081.

(22) Kutes, Y.; Zhou, Y.; Bosse, J. L.; Steffes, J.; Padture, N. P.; Huey, B. D. Mapping the Photoresponse of CH3NH3PbI3 Hybrid Perovskite Thin Films at the Nanoscale. *Nano Lett.* **2016**, *16* (6), 3434−3441.

(23) Wieghold, S.; Correa-Baena, J.-P.; Nienhaus, L.; Sun, S.; Shulenberger, K. E.; Liu, Z.; Tresback, J. S.; Shin, S. S.; Bawendi, M. G.; Buonassisi, T. Precursor Concentration Affects Grain Size, Crystal Orientation, and Local Performance in Mixed-Ion Lead Perovskite Solar Cells. *ACS Appl. Energy Mater.* **2018**, *1* (12), 6801−6808.

(24) Wieghold, S.; Tresback, J.; Correa-Baena, J.-P.; Hartono, N. T. P.; Sun, S.; Liu, Z.; Layurova, M.; VanOrman, Z. A.; Bieber, A. S.; Thapa, J.; Lai, B.; Cai, Z.; Nienhaus, L.; Buonassisi, T. Halide Heterogeneity Affects Local Charge Carrier Dynamics in Mixed-Ion Lead Perovskite Thin Films. *Chem. Mater.* **2019**, *31* (10), 3712−3721.

(25) Song, J.; Zhou, Y.; Padture, N. P.; Huey, B. D. Anomalous 3D Nanoscale Photoconduction in Hybrid Perovskite Semiconductors Revealed by Tomographic Atomic Force Microscopy. *Nat. Commun.* **2020**, *11* (1), 3308.

(26) Garrett, J. L.; Tennyson, E. M.; Hu, M.; Huang, J.; Munday, J. N.; Leite, M. S. Real-Time Nanoscale Open-Circuit Voltage Dynamics of Perovskite Solar Cells. *Nano Lett.* **2017**, *17* (4), 2554−2560.

(27) Ohmann, R.; Ono, L. K.; Kim, H.-S.; Lin, H.; Lee, M. V.; Li, Y.; Park, N.-G.; Qi, Y. Real-Space Imaging of the Atomic Structure of Organic−Inorganic Perovskite. *J. Am. Chem. Soc.* **2015**, *137* (51), 16049−16054.

(28) She, L.; Liu, M.; Zhong, D. Atomic Structures of CH3NH3PbI3 (001) Surfaces. *ACS Nano* **2016**, *10* (1), 1126−1131.

(29) Hieulle, J.; Wang, X.; Stecker, C.; Son, D.-Y.; Qiu, L.; Ohmann, R.; Ono, L. K.; Mugarza, A.; Yan, Y.; Qi, Y. Unraveling the Impact of Halide Mixing on Perovskite Stability. *J. Am. Chem. Soc.* **2019**, *141* (8), 3515−3523.

(30) Gallet, T.; Grabowski, D.; Kirchartz, T.; Redinger, A. Fermi-Level Pinning in Methylammonium Lead Iodide Perovskites. *Nanoscale* **2019**, *11* (36), 16828−16836.

(31) Ballard, J. B.; Carmichael, E. S.; Shi, D.; Lyding, J. W.; Gruebele, M. Laser Absorption Scanning Tunneling Microscopy of Carbon Nanotubes. *Nano Lett.* **2006**, *6* (1), 45−49.

(32) Scott, G.; Ashtekar, S.; Lyding, J.; Gruebele, M. Direct Imaging of Room Temperature Optical Absorption with Subnanometer Spatial Resolution. *Nano Lett.* **2010**, *10* (12), 4897−4900.

(33) Nienhaus, L.; Wieghold, S.; Nguyen, D.; Lyding, J. W.; Scott, G. E.; Gruebele, M. Optoelectronic Switching of a Carbon Nanotube Chiral Junction Imaged with Nanometer Spatial Resolution. *ACS Nano* **2015**, *9* (11), 10563−10570.

(34) Nienhaus, L.; Goings, J. J.; Nguyen, D.; Wieghold, S.; Lyding, J. W.; Li, X.; Gruebele, M. Imaging Excited Orbitals of Quantum Dots: Experiment and Electronic Structure Theory. *J. Am. Chem. Soc.* **2015**, *137* (46), 14743−14750.

(35) Gerstner, V.; Knoll, A.; Pfeiffer, W.; Thon, A.; Gerber, G. Femtosecond Laser Assisted Scanning Tunneling Microscopy. *J. Appl. Phys.* **2000**, *88* (8), 4851−4859.

(36) Lyubinetsky, I.; Dohnálek, Z.; Ukraintsev, V. A.; Yates, J. T. Transient Tunneling Current in Laser-Assisted Scanning Tunneling Microscopy. *J. Appl. Phys.* **1997**, *82* (8), 4115−4117.

(37) Kretschmann, E.; Raether, H. Notizen: Radiative Decay of Non Radiative Surface Plasmons Excited by Light. *Z. Für Naturforschung A* **1968**, *23* (12), 2135−2136.

(38) Carmichael, E. S.; Ballard, J. B.; Lyding, J. W.; Gruebele, M. Frequency-Modulated, Single-Molecule Absorption Detected by Scanning Tunneling Microscopy. *J. Phys. Chem. C* **2007**, *111* (8), 3314−3321.

(39) Nguyen, D.; Goings, J. J.; Nguyen, H. A.; Lyding, J.; Li, X.; Gruebele, M. Orientation-Dependent Imaging of Electronically Excited Quantum Dots. *J. Chem. Phys.* **2018**, *148*, 064701.

(40) Wang, S.; Chiang, N.; Guo, H.; Wattanatorn, N.; Barr, K. K.; Alexandrova, A. N.; Weiss, P. S. Photoinduced Carrier Generation and Distribution in Solution-Deposited Titanyl Phthalocyanine Monolayers. *Chem. Mater.* **2019**, *31* (24), 10109−10116.

(41) Nguyen, H. A.; Banerjee, P.; Nguyen, D.; Lyding, J. W.; Gruebele, M.; Jain, P. K. STM Imaging of Localized Surface Plasmons on Individual Gold Nanoislands. *J. Phys. Chem. Lett.* **2018**, *9* (8), 1970−1976.

(42) Wieghold, S.; Nienhaus, L.; Knoller, F. L.; Schweinberger, F. F.; Shepherd, J. J.; Lyding, J. W.; Heiz, U.; Gruebele, M.; Esch, F. Plasmonic Support-Mediated Activation of 1 Nm Platinum Clusters for Catalysis. *Phys. Chem. Chem. Phys.* **2017**, *19* (45), 30570−30577.

(43) Stark, J. Beobachtungen Über Den Effekt Des Elektrischen Feldes Auf Spektrallinien. I. Quereffekt. *Ann. Phys.* **1914**, *348* (7), 965−982.

(44) Brivio, F.; Frost, J. M.; Skelton, J. M.; Jackson, A. J.; Weber, O. J.; Weller, M. T.; Goñi, A. R.; Leguy, A. M. A.; Barnes, P. R. F.; Walsh, A. Lattice Dynamics and Vibrational Spectra of the Orthorhombic, Tetragonal, and Cubic Phases of Methylammonium Lead Iodide. *Phys. Rev. B* **2015**, *92* (14), 144308.

(45) Limmer, D. T.; Ginsberg, N. S. Photoinduced Phase Separation in the Lead Halides Is a Polaronic Effect. *J. Chem. Phys.* **2020**, *152* (23), 230901.

(46) Hsu, H.-C.; Huang, B.-C.; Chin, S.-C.; Hsing, C.-R.; Nguyen, D.-L.; Schnedler, M.; Sankar, R.; Dunin-Borkowski, R. E.; Wei, C.-M.; Chen, C.-W.; Ebert, P.; Chiu, Y.-P. Photodriven Dipole Reordering: Key to Carrier Separation in Metalorganic Halide Perovskites. *ACS Nano* **2019**, *13* (4), 4402−4409.

(47) Ballard, J. B.; Carmichael, E. S.; Shi, D.; Lyding, J. W.; Gruebele, M. Laser Absorption Scanning Tunneling Microscopy of Carbon Nanotubes. *Nano Lett.* **2006**, *6* (1), 45−49.

(48) Rose, V.; Shirato, N.; Bartlein, M.; Deriy, A.; Ajayi, T.; Rosenmann, D.; Hla, S.-W.; Fisher, M.; Reininger, R. XTIP − the World's First Beamline Dedicated to the Synchrotron X-Ray Scanning Tunneling Microscopy Technique. *J. Synchrotron Radiat.* **2020**, *27* (3), 836−843.

(49) Eames, C.; Frost, J. M.; Barnes, P. R. F.; O'Regan, B. C.; Walsh, A.; Islam, M. S. Ionic Transport in Hybrid Lead Iodide Solar Cells. *Nat. Commun.* **2015**, *6* (1), 7497.

(50) Drisdell, W. S.; Leppert, L.; Sutter-Fella, C. M.; Liang, Y.; Li, Y.; Ngo, Q. P.; Wan, L. F.; Gul, S.; Kroll, T.; Sokaras, D.; Javey, A.; Yano, J.; Neaton, J. B.; Toma, F. M.; Prendergast, D.; Sharp, I. D. Determining Atomic-Scale Structure and Composition of Organo-Lead Halide Perovskites by Combining High-Resolution X-Ray Absorption Spectroscopy and First-Principles Calculations. *ACS Energy Lett.* **2017**, *2* (5), 1183−1189.

(51) Tsai, H.; Liu, C.; Kinigstein, E.; Li, M.; Tretiak, S.; Cotlet, M.; Ma, X.; Zhang, X.; Nie, W. Critical Role of Organic Spacers for Bright 2D Layered Perovskites Light-Emitting Diodes. *Adv. Sci.* **2020**, *7*, 1903202.

(52) Wu, X.; Tan, L. Z.; Shen, X.; Hu, T.; Miyata, K.; Trinh, M. T.; Li, R.; Coffee, R.; Liu, S.; Egger, D. A.; Makasyuk, I.; Zheng, Q.; Fry, A.; Robinson, J. S.; Smith, M. D.; Guzelturk, B.; Karunadasa, H. I.; Wang, X.; Zhu, X.; Kronik, L.; Rappe, A. M.; Lindenberg, A. M. Light-Induced Picosecond Rotational Disordering of the Inorganic Sublattice in Hybrid Perovskites. *Sci. Adv.* **2017**, *3* (7), e1602388.

(53) Wang, K.; Rosenmann, D.; Holt, M.; Winarski, R.; Hla, S.-W.; Rose, V. An Easy-to-Implement Filter for Separating Photo-Excited Signals from Topography in Scanning Tunneling Microscopy. *Rev. Sci. Instrum.* **2013**, *84* (6), 063704.

(54) Guzelturk, B.; Winkler, T.; Van de Goor, T. W. J.; Smith, M. D.; Bourelle, S. A.; Feldmann, S.; Trigo, M.; Teitelbaum, S. W.; Steinrück, H.-G.; de la Pena, G. A.; Alonso-Mori, R.; Zhu, D.; Sato, T.; Karunadasa, H. I.; Toney, M. F.; Deschler, F.; Lindenberg, A. M. Visualization of Dynamic Polaronic Strain Fields in Hybrid Lead Halide Perovskites. *Nat. Mater.* **2021**, *20* (5), 618−623.

(55) Guzelturk, B.; Lindenberg, A. Dynamic Structural Views in Solar Energy Materials by Femtosecond Electron Diffraction. *MRS Bull.* **2021**, *46* (8), 704−710.

(56) Shih, M.-C.; Hsu, H.-C.; Lin, C.-C.; Huang, S.-K.; Chen, T.-P.; Tsai, Y.-H.; Chen, C.-C.; Chiu, Y.-P.; Chen, C.-W. Atomically Resolved Quantum-Confined Electronic Structures at Organic−Inorganic Interfaces of Two-Dimensional Ruddlesden−Popper Halide Perovskites. *Nano Lett.* **2021**, *21* (19), 8066−8072.

(57) Telychko, M.; Edalatmanesh, S.; Leng, K.; Abdelwahab, I.; Guo, N.; Zhang, C.; Mendieta-Moreno, J. I.; Nachtigall, M.; Li, J.; Loh, K. P.; Jelinek, P.; Lu, J. Sub-Angstrom Noninvasive Imaging of Atomic Arrangement in 2D Hybrid Perovskites. *Sci. Adv.* **2022**, *8* (17), eabj0395.